Experimental and numerical study on a novel dual-resonance wave energy converter with a built-in power take-off system

Zhongfei Chen[a], Binzhen Zhou[a,b*], Liang Zhang[a,*], Can Li[a], Jun Zang[c], Xiongbo Zheng[d], Jianan Xu[e], Wanchao Zhang[f]

[a]*College of Shipbuilding Engineering, Harbin Engineering University, Harbin 150001, China*

[b]*Key Laboratory of Renewable Energy, Guangzhou Institute of Energy Conversion, Chinese Academy of Sciences, Guangzhou 510640,, China*

[c]*Department of Architecture and Civil Engineering, University of Bath, Bath, BA2 7AY, UK*

[d]*College of Science, Harbin Engineering University, Harbin 150001 China*

[e]*College of Mechanical and Electrical Engineering, Harbin Engineering University, Harbin 150001 China*

[f]*School of naval structure and ocean engineering, Jiangsu University of Science and Technology, Zhenjiang 212003, China*

Abstract

A new concept of point-absorber wave energy converter (WEC) with a waterproof outer-floater and a built-in power take-off (BI-PTO) mechanism, named Dual-Resonance WEC (DR-WEC), is put forward and investigated by experiments and numerical simulations. The BI-PTO mechanism includes spring, sliding-mass and damping systems, where the spring system is the most complicated and should be designed specially. A 1:10 scale model is designed for the experiments. The mechanical performance of the BI-PTO system is investigated by a bench test. The results have shown that the design is feasible, and the added inertia effect of the BI-PTO has a negative influence on the power output. The average mechanical efficiency of the BI-PTO is 65.8% with maximum up to 80.0%. The motion and power responses of the DR-WEC are studied by a wave tank experiment and a linear numerical model with corrected mechanical added mass and viscosity. The viscous added mass and damping correction coefficients are obtained by a free decay test. The good agreement between the experimental measurements and numerical simulations has indicated that the present numerical model with corrections is of enough accuracy and the effects of mooring system and other degree of freedoms on the heave motion and power responses can be ignored.

Key words: Wave energy converter; Dual-resonance; Built-in power take-off system; Viscous correction; Motion response; Capture width ratio

*Corresponding author.

E-mail addresses: zhoubinzhen@hrbeu.edu.cn (B.Z. Zhou), zhangliang@hrbeu.edu.cn (L. Zhang).

1. Introduction

Wave energy is one of ocean renewable energy with huge reserves. Approximately, it could meet the electricity requirement of most countries that have enough coastline, if it is extensively exploited [1]. Generally, wave energy converter (WEC) techniques can be classified into attenuator, terminator, and point-absorber (PA) [2]. Extensive reviews can be found in [2-5]. A point-absorber WEC is convenient for array arrangement because of its small dimension relative to the encounter wavelength, and this type is very efficient in terms of wave-power absorption per unit volume [6]. These features make it perfectly suitable for the ocean areas with relatively low wave energy density such as the Chinese adjacent seas [7]. Even though, in these areas, the wave energy may not be sufficient enough to steadily supply the power for main-land grids, it could be an effective supplement for microgrids of islands, oil platforms, or other offshore marine structures [8].

There is one type of configuration of WEC that all power take-off (PTO) systems are built inside a water-proof outer-floater, such as, SEAREV (France) [9], Penguin (UK) [10], GyroPTO (Denmark) [11], and PS Frog Mk5 (UK) [12], etc. The wave energy is absorbed by the outer-floater and converted into mechanical energy, and then the PTO converts it to a more usable type of energy (e.g., electrical energy). Compared with many existing or proposed concepts that have moving mechanical parts immersed in the water, this kind of configuration could increase the reliability, reduce the difficulty of maintenance, and is good for the survivability in the harsh environments. The cost of a traditional point-absorber WEC is sensitive to the water depth, because it needs a fixed structure on sea-bottom or on shore as the reaction for the PTO. However, for a point-absorber WEC with a built-in PTO (BI-PTO), the PTO is built inside the outer-floater. Therefore, it is more cost-effective in term of water depth, because only a slacking mooring system is in need to overcome drift forces.

For a point-absorber WEC with a BI-PTO, the hydrodynamic properties of the outer-floater are relatively easy to compute, while the key issue is the design of a feasible BI-PTO system. The PTO consists of an inertial reaction body to form a relative motion with respect to the outer-floater. Generally, the internal reaction body has three types, namely pendulum (vertical or horizontal axis), gyroscope, and sliding-mass (see examples in [9-12]). The pendulum and gyroscope can work in pitch or roll only, and the gyroscope needs a high rotational speed which may be bad for the fatigue life of the system. The

sliding-mass is working in the translational motion and the mechanical structure is relatively simple to design. The heave motion is more favorable for a point-absorber WEC because an axisymmetric out-floater can be applied to reduce the sensitiveness of wave directions. Therefore, the DR-WEC works in heave and adopts the sliding-mass as the internal reaction body.

The installing and testing of a WEC is difficult and expensive in the real marine environment, so that a device should be simulated and tested in small-scale first [13]. Ning et al. [14] tested a pile-restrained WEC-type floating breakwater, and the wave energy capture ability and the breakwater ability were studied. A coaxial-cylinder WEC was studied experimentally and numerically by Son et al. [15]. Liu et al. [16] studied wave overtopping behaviors of a circular ramp overtopping WEC experimentally. An experiment of a 1:30 scale WaveCat was performed by Allen et al. [17], which formed the basis for future development and optimization. The key issue of a point-absorber WEC with a BI-PTO is the design of the PTO mechanism which is required to be tested and validated on the bench (which is normally a dry-test facility) first before testing of the whole system in the water, due to the complexity and the high cost of a PTO system [13]. The specialized test benches are able to simulate the wave excited motion of the outer-floater, so that the feasibility, reliability, and mechanical performance of PTOs can be validated and tested. Many researchers had conducted dry bench tests for PTOs. Dellicolli et al. [18] tested a permanent-magnet synchronous tubular linear generator for PA-WECs. The design and analysis were reported based on the experimental results on a rotating simulation test bench. Lasa et al. [19] designed and tested a hydraulic PTO on the bench to validate the dynamic performance. The experimental results were used for the improvement of an in-house numerical simulation model. Antolín-Urbaneja et al. [20] studied a hydraulic PTO device which consists of a double-acting hydraulic cylinder. The test results on the bench showed good correlations to that of the simulations.

In the present paper, a novel DR-WEC working in heave motion with a BI-PTO system is put forward. A sliding-mass is placed inside the outer floater and the relative heave motion between them makes the PTO system capture energy. The BI-PTO system composed of spring, sliding-mass, and damping systems is specially designed for the DR-WEC. A 1:10 scale model is constructed. A special bench test was firstly carried out to study the feasibility of the design and the mechanical performance of the BI-PTO system. Furthermore, the motion and power responses of the DR-WEC in regular waves are investigated by the experiment conducted in the wave tank at Harbin Engineering University. Meanwhile, a linear numerical

model considering the mechanical added mass and viscous corrections is developed to study the hydrodynamic performance of the DR-WEC only in heave motion. The comparison with the experimental results is made to show the accuracy of the numerical model and the effect of mooring system and other degree of freedoms.

2. DR-WEC concept

The DR-WEC concept is demonstrated in Fig.1. There are two sets of mass-spring-damping in the DR-WEC. The first is the mass of the outer-floater, spring of the hydrostatic restoring effect, and hydrodynamic damping of the floater. The second is from the PTO mechanism which is inside the outer-floater. Namely, the internal spring, the sliding-mass, and the damping of the generator. Because of the existence of these two sets of mass-spring-damping, the system has two undamped resonance frequencies. Therefore, we name this new WEC concept as the DR-WEC. The DR stands for the "Dual Resonance". By manipulating the parameters of the internal one can change these resonance frequencies. This gives a possibility that we can match the one of the resonance frequencies to the wave encounter frequency to enhance the wave power absorbing ability.

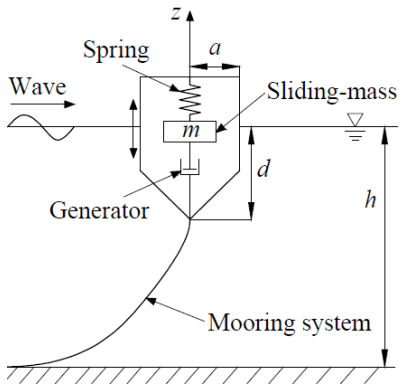

Fig.1. The general schematics of the DR-WEC.

The outer-floater is axisymmetric to reduce the sensibility to wave directions. The conical bottom is to diminish the viscous dissipation, based on the research results in [21]. The radius and draft are a and d, respectively. The water depth is h. The hydrodynamic performance of the outer-floater can be evaluated by model tests in the wave tank with the consideration of the fluid viscosity.

3. Model design

3.1. Outer-floater

The outer-floater is made of the 6061 high tensile aluminum alloy. The thickness is 3.0mm. The upper part is a vertical cylinder and the lower part is a conical bottom, which is designed to reduce the viscous dissipation. At the tip of the conical bottom, a steel ring is attached to link the mooring system. The detailed geometry parameters can be found in Fig.2.

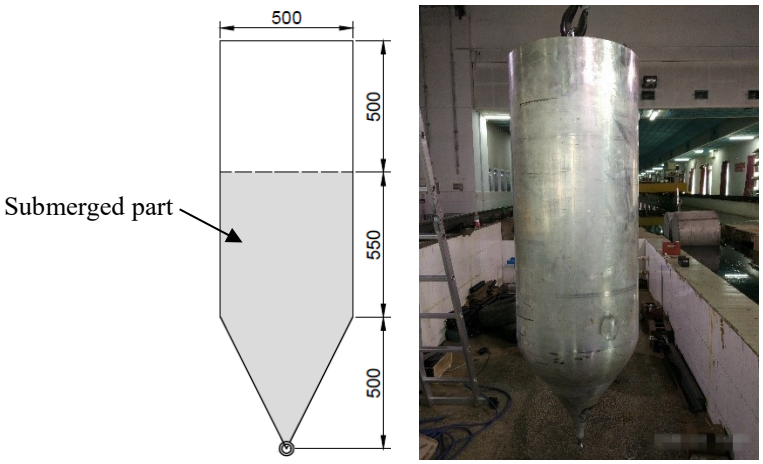

(a) (b)

Fig.2. Schematic (a) and photograph (b) of the floater of the DR-WEC [unit: mm].

3.2. BI-PTO

This section describes the design and assembly of the BI-PTO mechanisms. There are three parts in the BI-PTO, i.e., the spring system, mass system, and damping system, among which the spring system is the most complex part to design, while the mass and damping systems are relatively easier.

3.2.1. Spring system

The spring system has two major functions: One is achieving the variable spring coefficient, and the second is neutralizing the gravity force of the sliding-mass. The design sketch of the spring system is illustrated in Fig.3. It consists of a fixed spring (tension spring), wire ropes, and a stepped pulley. The radius ratio r_1/r_2 of the stepped pulley is set as 1/3.6, and the different spring coefficient K_m is achieved by changing the fixed spring in the present experiment. In the real application, a possible solution is using an automatic gearbox which can provide different gear ratio (namely, different r_1/r_2) to vary K_m automatically.

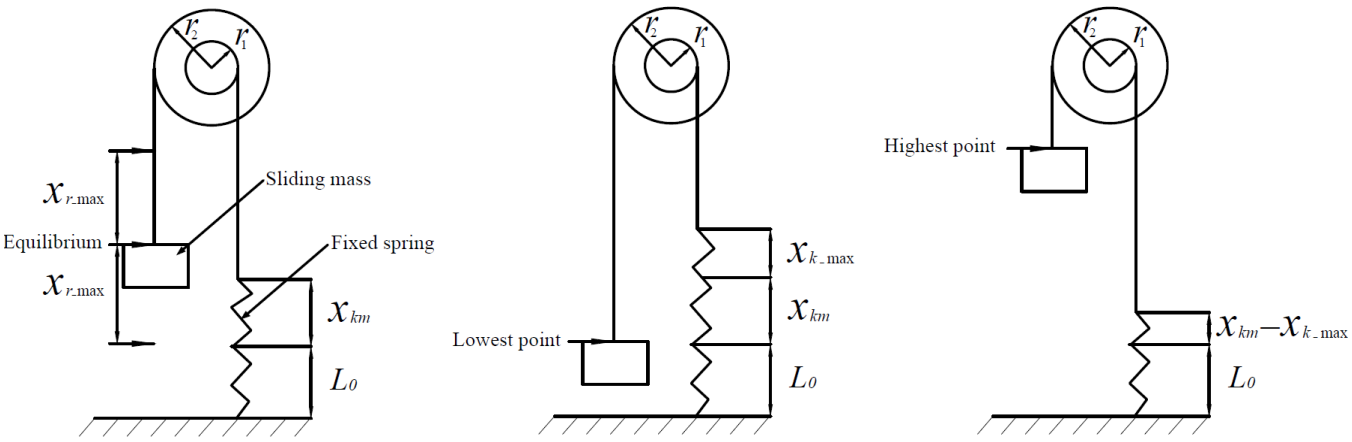

(a) equilibrium (b) lowest (c) highest

Fig.3. The design sketch of the spring system and the three special positions of the sliding-mass during operation.

When the sliding-mass locates at the equilibrium position (Fig.3(a)) and the lowest position (Fig.3(b)), the moment equilibrium equations are

$$\begin{cases} mgr_2 = K_0 x_{k,m} r_1 \\ \left(mg + K_m x_{r,\max}\right) r_2 = K_0 \left(x_{k,\max} + x_{k,m}\right) r_1 \end{cases} \tag{1}$$

where K_0 is the spring constant of the fixed spring. $x_{k,m}$ is the elongation of the fixed spring to neutralize the gravity of the sliding-mass. $x_{r,\max}$ and $x_{k,\max}$ are the maximum positions of the sliding-mass and the corresponding fixed spring elongation, respectively. Combining Eq.(1) and the relationship $r_1 x_{r,\max} = r_2 x_{k,\max}$, the relationship between the K_m and K_0 can be derived by

$$K_m = \left(\frac{r_1}{r_2}\right)^2 K_0 \tag{2}$$

The stepped pulley is demonstrated in Fig.4. There are spiral grooves on the big and small pulleys to guide the wire ropes which are winded on them. The green pulley is aligned with the small pulley to lead the wire rope on the small pulley to the spring. The wire rope on the big pulley is linked with the sliding-mass. There are four bearings for one such stepped pulley system, and all of them are chosen as ceramic bearings. Compared with normal bearings made by steel, the friction coefficients of the ceramic bearings are very small. By supplementary experiments, the equivalent friction coefficients of the whole stepped pulley system with steel bearings and ceramic bearings are 0.06 and 0.02, respectively. The geometrical parameters of the different components of the stepped pulley system are shown in Table 1.

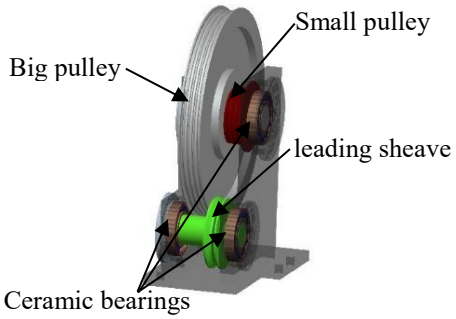

Fig.4. The rendering of the stepped pulley.

Table 1 Diameters of the components of the stepped pulley system [mm].

Big pulley	180.0
Small pulley	50.0
Leading sheave	50.0
Shafts	20.0
Wire ropes	3.0

The spring system should satisfy three requirements. First, the fixed spring should be in tensile state all the time, because the fixed stepped pulley system cannot be compressed. When the sliding-mass is at the highest position (Fig.3(c)), the stretch of the fixed spring is the smallest. In other words, if the fixed spring has non-zero stretch when the sliding-mass is at the highest position, the fixed spring can be in tensile state all the time during the operation. Second, the allowable elongation ΔL_a of the fixed spring should be large enough when the sliding-mass is at the lowest position (Fig.3(b)). Third, the original length of the fixed spring L_0 should be small enough due to the limited vertical space of the waterproof outer-floater of the DR-WEC. The allowable vertical space inside the outer-floater is set to two times of the allowable maximum amplitude of the relative motion, i.e. $2x_{r,\max}$=0.8m. These three requirements are quantitatively shown in the following equation.

$$\begin{cases} x_{k,m} - x_{k,\max} \geq 0 \\ \Delta L_a \geq x_{k,m} + x_{k,\max} \\ L_0 + x_{k,m} + x_{k,\max} \leq 2x_{r,\max} \end{cases} \tag{3}$$

If there are N sets of stepped pulley spring system that are installed in parallel, combining Eq.(1) and (2), the relation between the K_m and K_0 as well as the limitations in Eq.(3) can be concluded as

$$\begin{cases} K_m = N\left(\dfrac{r_1}{r_2}\right)^2 K_0 \\ K_0 \le \dfrac{1}{x_{r,\max}} \dfrac{N}{mg}\left(\dfrac{r_1}{r_2}\right)^2 \\ \Delta L_c \ge \dfrac{mgr_1}{K_m r_2} + \dfrac{r_1}{r_2} x_{r,\max} \\ L_0 \le \left(2 - \dfrac{r_1}{r_2}\right) x_{r,\max} - \dfrac{mgr_1}{K_m r_2} \end{cases} \tag{4}$$

The non-dimensional spring ratio is defined as $\bar{s} = K_m / K_3$, where $K_3=\rho g\pi a^2$ is the hydrostatic restoring coefficient of the outer-floater, ρ is the water density and g is the gravitational acceleration. Accordingly, the designed $\bar{s}$ and corresponding K_m and K_0 are illustrated in Table 2.

Table 2 The spring ratio, equivalent spring constants of the spring system, and the spring constants of the fixed spring.

No.	$\bar{s}$	K_m [N/m]	K_0 [N/m]
1	0.29	555.8	3601.8
2	0.39	747.5	4843.9

3.2.2. Sliding-mass system

For the internal sliding-mass, shown in Fig.5, we use the distributed metal disks (0.45kg each) which are made by lead to vary the mass. The lead disks are placed on a metal base that weighted 22.0kg. The maximum mass of the sliding-mass is 58.0kg with 80 lead disks. The non-dimensional mass ratio is defined as $\bar{m} = m / M$, where m is the mass of the sliding-mass and M is the mass of the whole DR-WEC system. Thus, the varying range of the mass ratio $\bar{m}$ is from 0.15 to 0.40. The sliding-mass is able to slide on two vertical axes by linear bearings. The extreme stroke of the sliding-mass is 0.8m which is confined by the vertical space inside the outer-floater, i.e., the maximum relative motion amplitude $x_{r,\max}$ equals to 0.4m. On the top surface of the base, there are two linkers which are used for the connection with the spring system. Another two linkers used for the damping system locate at the center of the top and bottom surfaces of the base, respectively.

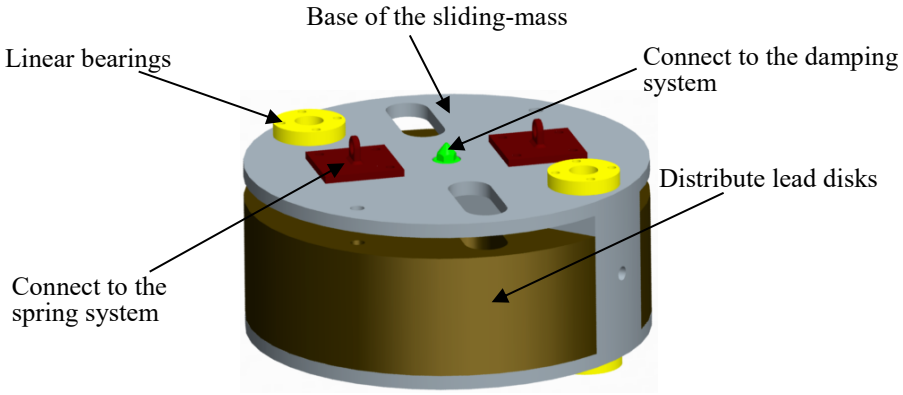

Fig.5. The rendering of the sliding-mass.

3.2.3. Damping system

The damping of a generator is relatively easy to manipulate. Son et al. [15] changed the damping of a permanent magnet linear generator by varying the air gap or the load resistance. The damping of a hydraulic system is able to be controlled by throttle valves [22]. Furthermore, like the spring system, we can also use the gear box (installed on the shaft of the generator) to alter the damping.

In a full-scale DR-WEC, a permanent magnet synchronous generator (PMSG) will be used to convert the relative motion between the internal sliding-mass and the outer-floater into electricity. In this study, as shown in Fig.6, the damping of the generator is simulated by a permanent electromagnetic brake which is similar to the one used in [14]. The non-dimensional damping ratio is defined as $\overline{d} = C_g/\lambda_{33res}$, where λ_{33res} is the hydrodynamic damping of the outer-floater at its resonance frequency. The brake can provide variable damping (16.8kg/s to 43.2kg/s, which corresponds to $\overline{d}$ =0.8 to 2.1) for the sliding-mass by the controller. The damping system is connected to the sliding-mass by wire ropes that are winded on the double-groove pulley. Because the movement of the sliding-mass is reciprocating, the pulley has to consist of two grooves to wind the wire ropes in order to prevent overlapping. A 1:1 orthogonal gear box is connected between the pulley and the brake to save the space.

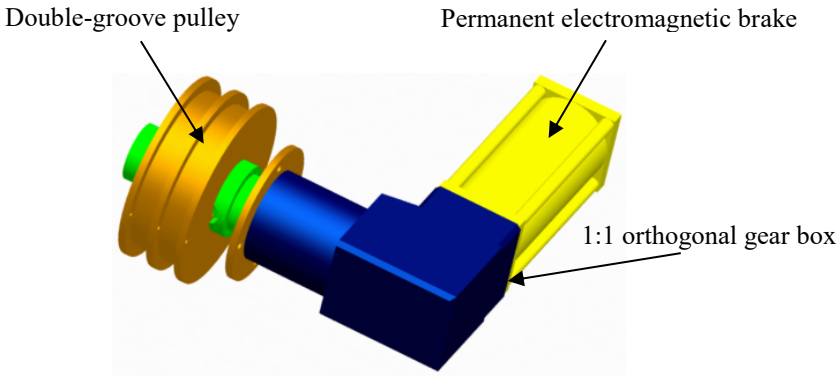

Fig.6. The rendering of the damping system.

3.2.4. Assembly

The BI-PTO is installed inside this outer-floater. The spring, sliding-mass, and damping system of the built-in BI-PTO are assembled as illustrated in Fig.7. The main frame consists of upper deck, lower deck, and two circular reinforce ribs which are welded onto the inner surface of the outer-floater. The upper deck (or lower deck) is connected with the reinforce ribs by screws. The decks, reinforce ribs and outer-floater form a rigid frame structure. All components are connected to these two decks. Therefore, the PTO loads first act on these decks, then transfer to the reinforce ribs and to the outer-floater.

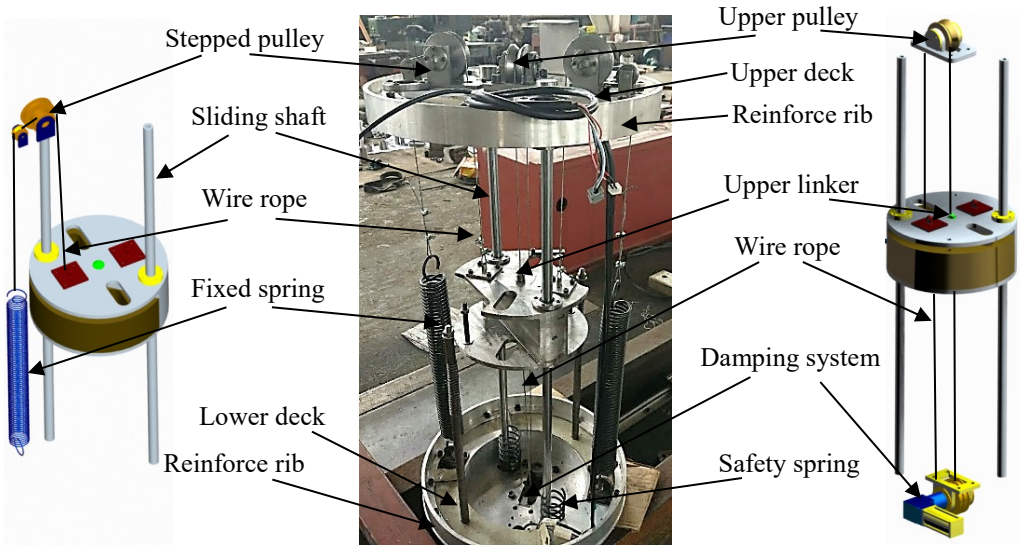

(a) Spring & mass (b) Whole PTO system (c) Damping & mass

Fig.7. The assembly of the BI-PTO system.

4. Methodology

4.1. Motion and power response on the bench

During the motion of the sliding-mass, other parts like the pulleys, wire ropes, shafts, etc. are also moving. Therefore, an added term $f_{\mu,mech}=-\mu_{mech}\ddot{z}$ should be considered in the motion equation Eq.(5) to include the inertia effect of moving parts (except the sliding-mass). By Newton's second law, the motion equation of the sliding-mass becomes

$$m\ddot{z} = f_{C,total} + f_K + f_{\mu,mech} \tag{5}$$

where $f_{C,total}=-C_{total}\dot{z}$ is the damping force of the whole PTO system. In reality, the friction force should be Coulomb friction. However, to conduct the linear frequency domain analysis in our paper, we use this linearized term to describe it. The linearized total damping C_{total} consists of the linearized mechanical

friction damping C_{mech} and the linearized electromagnet damping C_g, and C_{total} can be calculated by Eq.(13). $f_K=-K_m x_r$ is the spring force from the spring system. x_r, $\dot{x}_r$ and $\ddot{x}_r$ are the relative displacement, velocity and acceleration between the sliding-mass and the outer-floater, respectively. $x_{3m}=x_r+x_{3f}$, $\dot{x}_{3m}$, $\dot{x}_{3m}$ and $\ddot{x}_{3m}$ are the displacement, velocity and acceleration of the sliding-mass, respectively. x_{3f}, $\dot{x}_{3f}$ and $\ddot{x}_{3f}$ are the displacement, velocity and acceleration of the outer-floater, respectively.

The resonance period T_{res} of the BI-PTO has nothing to do with the outer-floater motion. By fixing the outer-floater and ignoring the influence of damping, Eq.(5) can be converted into the homogeneous motion equation

$$\left(m+\mu_{mech}\right)\ddot{x}_r+K_m x_r=0 \tag{6}$$

The resonance period T_{res} of the sliding-mass can be derived as

$$T_{res}=2\pi\sqrt{\frac{m+\mu_{mech}}{k_m}} \tag{7}$$

Clearly, the existence of μ_{mech} increases the resonance period T_{res}. On the other hand, we can calculate μ_{mech} by T_{res} which can be achieved from the response curves (e.g., Fig.13) by experiments.

$$\mu_{mech}=\frac{4\pi^2}{T_{res}^2 K_m}-m \tag{8}$$

As illustrated from Eq.(8), μ_{mech} is associated with the sliding-mass and spring. By setting C_g=0.0kg/s, μ_{mech} is shown in Table 3 for different PTO parameters. The mean μ_{mech} is 4.79kg. By nondimensionalization as $\bar{\mu}_{mech}=\mu_{mech}/M$, $\bar{\mu}_{mech}$ equals to 0.033. The mechanical added mass is caused by the moving parts (except the sliding-mass), and these parts are the same for different cases. Therefore, the differences of μ_{mech} are small for different cases (Table 3).

Table 3 The mechanical added mass for different PTO parameters.

m [kg]	K_m [N/m]	C_g [kg/s]	T_{res} [s]	μ_{mech} [kg]
35.5	555.8	0.0	1.69	4.91
44.5	555.8	0.0	1.78	4.75
35.0	747.5	0.0	1.42	4.71

The mechanical efficiency η is defined as the ratio of the absorbed power P_m by the damping system

and the total consumed power P_{total} by the whole PTO system, i.e. $\eta=P_m/P_{total}\times 100\%$.

Under the harmonic motion hypothesis, the power absorbed by the damping system is

$$P_m = \frac{1}{2} C_g \omega^2 \left|\hat{x}_r\right|^2 \tag{9}$$

The power consumed by the whole system is

$$P_{total} = \frac{1}{2} C_{total} \omega^2 \left|\hat{x}_r\right|^2 \tag{10}$$

where $\hat{x}_r$ is the amplitude of the relative motion. Accordingly, the mechanical efficiency can be written in the form of

$$\eta = \frac{C_g}{C_{total}} \times 100\% \tag{11}$$

Clearly, the efficiency is equal to the ratio of C_g and C_{total}. C_g is rated by a supplementary test in advance, while C_{total} is needed to be calculated by the relative motion x_r and floater motion x_f.

Through some rearrangement, the motion equation Eq.(5) can be expressed as

$$\left(m+\mu_{mech}\right)\ddot{\quad} \quad \dot{\quad} \quad \ddot{\quad} \tag{12}$$

Eq.(12) reveals that the motivation to move the sliding-mass is the inertia force $-m\ddot{\quad}$, which determines the amount of energy transported from the outer-floater into the sliding-mass. The motion provided by the linear motor is harmonic $x_{3f}(t)=\mathrm{Re}\left\{\hat{x}_{3f}e^{i\omega t}\right\}$. Put it into Eq.(12), the total damping C_{total} can be derived as

$$C_{total} = \omega m \frac{\left|\hat{x}_{3f}\right|}{\left|\hat{x}_r\right|}\sqrt{1-\left[\left(\frac{-\omega^2\mu_{mech}+k_m}{\omega^2 m}-1\right)\frac{\left|\hat{x}_r\right|}{\left|\hat{x}_{3f}\right|}\right]^2} \tag{13}$$

To justify the correctness of Eq.(13), we put the results of C_{total} back to the motion equation and the numerical motion results can be found in Fig.8. It is illustrated that the numerical results match well with the experimental measurements. Moreover, we add the detailed derivation procedure in Appendix A.

4.2. Motion and power responses in waves

Bachynski et al. [23] argued that a slack mooring system only affected the pitch and surge motions

at a very low frequency and had little influence on the heave motion. Thus, the effect of the mooring system is neglected in the present numerical analysis. The motion equation of the DR-WEC in heave under linear waves is

$$\begin{cases} (M-m)\ddot{x}_{3f} = f_{e3} + f_r + f_h - f_{C,total} - f_K - f_{\mu,mech} \\ m\ddot{x}_{3m} = f_{C,total} + f_K + f_{\mu,mech} \end{cases} \tag{14}$$

where f_{e3} is the wave excitation force in heave and it equals to $\mathrm{Re}\{A_w X_3 e^{-i\omega t}\}$ for linear regular waves. A_w is the wave amplitude, and X_3 is the wave excitation force per unit wave amplitude. $f_r = -\mu_{vis}\ddot{x}_{3f} - \lambda_{vis}\dot{x}_{3f}$ is the wave radiation force. $f_h = -K_3 x_{3f}$ is the hydrostatic restoring force. Eq.(14) can also be written in the matrix form

$$\begin{bmatrix} M-m+\mu_{vis}+\mu_{mech} & -\mu_{mech} \\ -\mu_{mech} & m+\mu_{mech} \end{bmatrix} \begin{Bmatrix} \ddot{x}_{3f} \\ \ddot{x}_{3m} \end{Bmatrix} + \begin{bmatrix} \lambda_{vis} & 0 \\ 0 & 0 \end{bmatrix} \begin{Bmatrix} \dot{x}_{3f} \\ \dot{x}_{3m} \end{Bmatrix} + \begin{bmatrix} K_m & -K_m \\ -K_m & K_m \end{bmatrix} \begin{Bmatrix} x_{3f} \\ x_{3m} \end{Bmatrix} = \begin{Bmatrix} f_{e3} \\ 0 \end{Bmatrix} \tag{15}$$

The solution of Eq.(15) in the frequency domain can be represented by the RAOs of the floater motion RAO_f and relative motion RAO_r.

$$\begin{cases} \mathrm{RAO}_f \equiv \left| \dfrac{\hat{x}_{3f}}{A_w} \right| \\ \mathrm{RAO}_r \equiv \left| \dfrac{\hat{x}_r}{A_w} \right| \end{cases} \tag{16}$$

where $\hat{x}_{3f}$ is the amplitude of the floater motion.

The capture width ratio is defined as

$$\bar{C}_w \equiv \frac{P_M}{P_W \cdot 2a} \cdot \eta \tag{17}$$

where P_M is the absorbed power by the WEC (same as Eq.(9)) and $P_W = \rho g A_w^2 V_g/2$ is the wave-power transportation per unit wave crest. V_g is the wave group velocity (Eq.(18)). η is mechanical efficiency of the BI-PTO system, as defined in Eq.(11).

$$V_g = \frac{1}{2}\frac{g}{\omega}\tanh(k_0 h)\left[1 + \frac{2k_0 h}{\sinh(2k_0 h)}\right] \tag{18}$$

where k_0 is the wave number.

Due to the existence of μ_{mech}, the inertia forces of both outer-floater $(M-m+\mu_{vis}+\mu_{mech})\ddot{x}_f$ and internal sliding-mass $(m+\mu_{mech})\ddot{x}_r$ increase. Moreover, two coupled terms $-\mu_{mech}\ddot{x}_f$ and $-\mu_{mech}\ddot{x}_r$ are shown up. That is, the inertia forces are not independent, but are coupled due to the inertia effect of the moving parts (except the sliding-mass) in the BI-PTO system. As illustrated in Fig.8, without the consideration of μ_{mech}, the motion response deviates from the experimental data obviously (taken m=35.5kg, K_m=555.8N/m, C_g=0.0kg/s as an example). After adopting Eq.(14) to consider the μ_{mech}, the theoretical results match the experimental data very well, especially the amplitude and the location of the response peak (Fig.8).

Practically, μ_{mech} is inevitable due to the existence of other moving parts in the BI-PTO mechanism. Fig.9 reveals that as μ_{mech} increases, the amplitudes of the motion and power responses at the lower frequency peak decrease, while at the higher frequency peak increase. The frequencies of both the lower and higher peaks become smaller. Normally, the motion and power response at lower frequency peak are larger than that at the higher frequency peak, as illustrated in Fig.9 and Fig.10. In addition, waves with lower frequency tend to have more energy [7]. Consequently, the effect of μ_{mech} on the motion and power response of the DR-WEC is negative. In practice, μ_{mech} should be as small as possible.

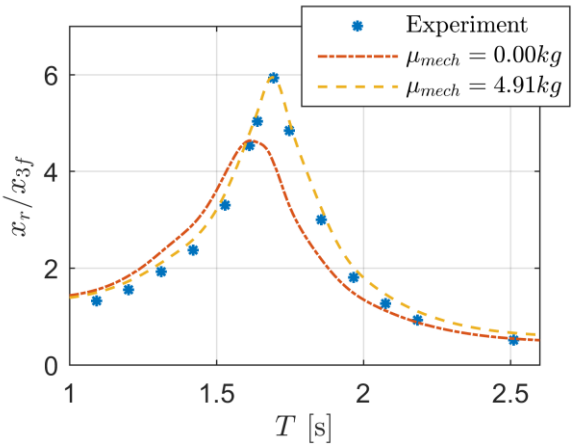

Fig.8. The motion response comparison with and without the mechanical added mass when m=35.5kg, K_m=555.8N/m, C_g=0.0kg/s.

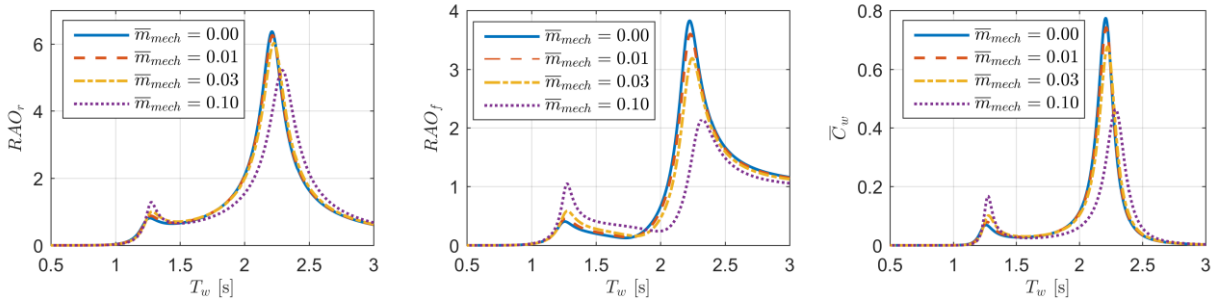

(a) Relative motion RAO (b) Floater motion RAO (c) Capture width ratio

Fig.9. Motion and power response for different mechanical added mass with $\overline{m}$ =0.30, $\overline{s}$ =0.29, and $\overline{d}$ =1.0.

The examples of the motion and power responses of the DR-WEC are shown in Fig.10 for different BI-PTO parameters. The dimensions of the example outer-floater are diameter 2a=0.5m, draft d=0.75m. The water depth is h=3.5m. The non-dimensional wave frequency is defined as $\overline{\omega} = \omega\sqrt{d/g}$. As mentioned in Section 2, the DR-WEC has two sets of mass-spring-damping system. The sliding-mass and the outer-floater together form the "dual resonance" system. The system has two distinct frequencies. Because both sliding-mass and the outer-floater are part of one system, so the motion responses of sliding-mass and the outer-floater have the same resonance frequencies. Moreover, as illustrated in Fig.10, one of these two resonance frequencies is smaller than the resonance frequency of the outer-floater ω_3, while the other is larger than that. With the PTO parameters varying, the response characteristics (both the resonance frequencies and the response amplitudes) of the DR-WEC are changing. Namely, the DR-WEC has the potential to adopt itself to different wave environment by manipulating the PTO parameters for better wave energy absorption.

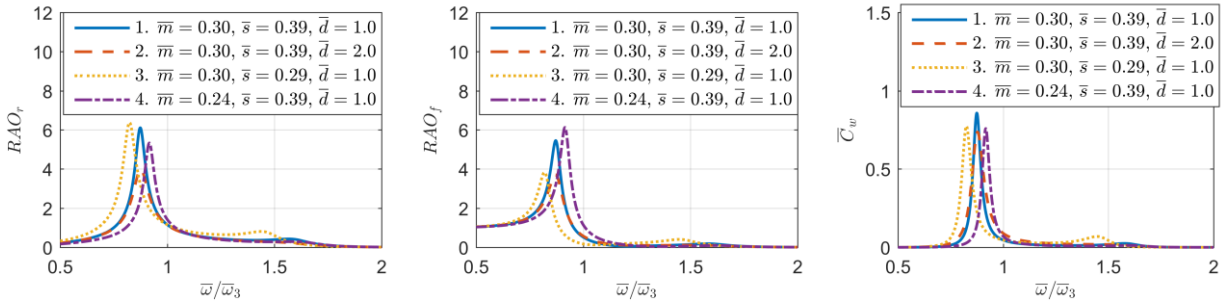

(a) Relative motion RAO (b) Floater motion RAO (c) Capture width ratio

Fig.10. Examples of the motion and power responses of the DR-WEC, with 2a=0.5m, d=0.75m, and h=3.5m.

5. Experiments

5.1. Experimental facilities

5.1.1. Test bench

To validate the performance and dynamic characteristics, the BI-PTO is needed to be tested on a special designed bench (Fig.11.) which is aimed to simulate the wave excited motion of the outer-floater. The main frame is made up of square steel. Four pulleys were set at the four corners. Then a closed loop was established by wire ropes with the test model, balance weight, and linear motor. The BI-PTO shown in Fig.7 was installed inside the outer-floater which mounted to the retaining frame. The balance weight at the right side was to neutralize the gravity force of the test model and the retaining frame at the left side. A linear motor was at the bottom of the main frame to provide linear reciprocating motion (harmonic motion). The ranges of the motion amplitude and period were 0.0-100.0mm and 0.8-2.5s, which corresponded to the wave making ability of the wave maker in the wave tank of Harbin Engineering University.

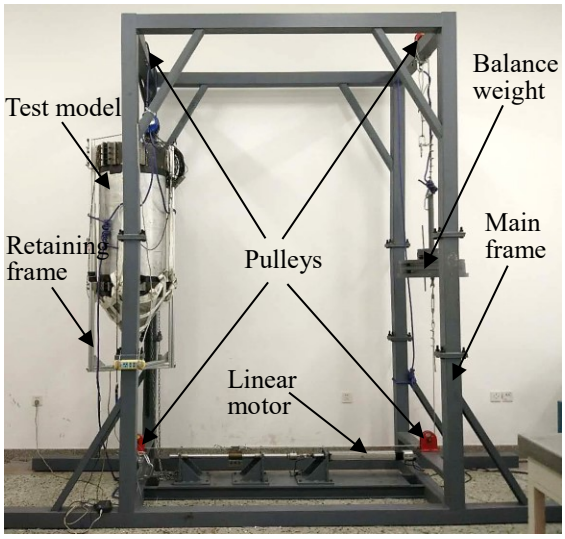

Fig.11. The test bench with test model in position.

5.1.2. Wave tank

The wet test of the DR-WEC was conducted in a wave tank at Harbin Engineering University, as shown in Fig.12. The length, width, and depth of the wave tank is 108.0m, 7.0m, and 3.5m, respectively. A flap-type wave maker with eight panels was installed at one end of the tank, which can generate regular waves with wave periods in the range of 0.4s to 4.0s and the maximum wave height 0.4m. A wave-

absorbing beach was located at the other end to reduce the wave reflection. The DR-WEC was put at the test location, which was 35.0m away from the wave-maker and the transverse center of wave tank.

Fig.12. Wave tank, trailer, and wave maker at Harbin Engineering University.

5.2. Bench test for the BI-PTO

The motion of the outer-floater $x_{3f}(t)$ and the relative motion $x_r(t)$ were measured by two linear potentiometers which were mounted on the main frame and the upper deck inside the floater, respectively. The rotating speed $n(t)$ and torque $T_q(t)$ of the electronic brake could be read on the controller, so that the instantaneous power on the brake shaft could be calculated as $P_m(t)=n(t)T_q(t)$.

5.2.1. Response characteristics

The examples of the time histories of $x_{3f}(t)$, $x_r(t)$ and instantaneous power $P_m(t)$ are shown in Fig.13 (a) and (b) (taken m=44.5kg, K_m=555.8N/m, C_g=27.3kg/s, and period T=1.8s as an example). The input $x_f(t)$ is harmonic, while the output $x_r(t)$ and $P_m(t)$ need some time to grow from zero to the stable state. In the following discussions, these time-domain data are transformed into frequency-domain results using the stable state data.

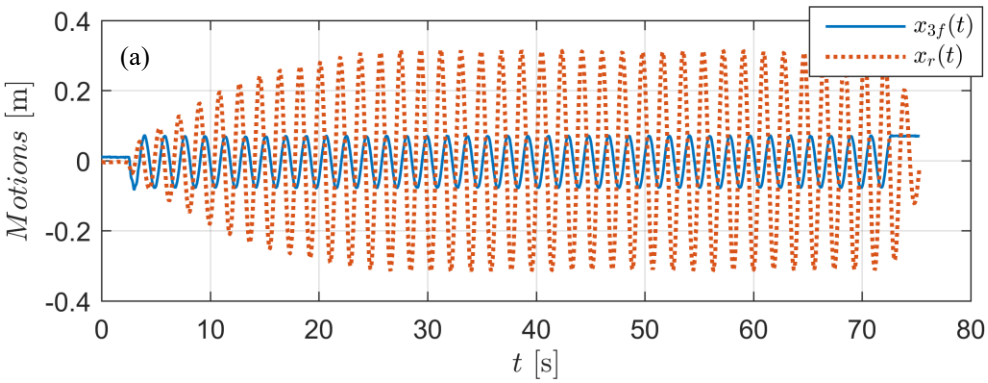

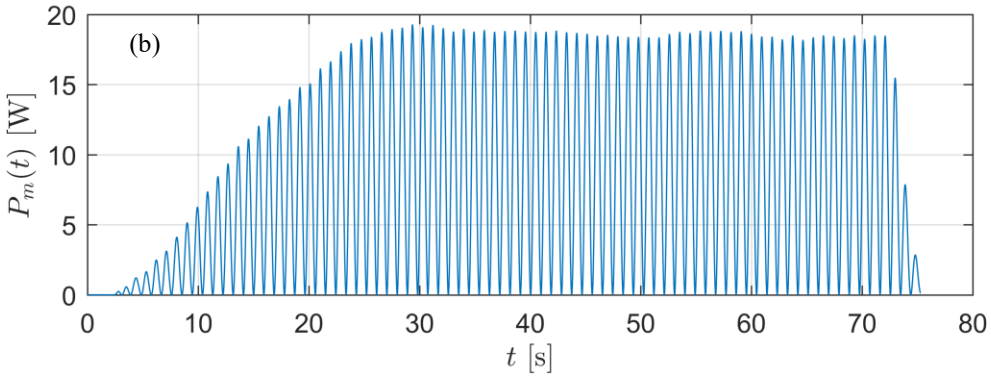

Fig.13. Examples of the time histories of the motions (a) and power (b) when m=44.5kg, K_m=555.8N/m, C_g=27.3kg/s, and T=1.8s.

Fig.14 shows the influence of the parameters of the BI-PTO system on the motion and power response, which has only one peak due to the outer-floater motion is given. The line 3 and 4 demonstrate that the damping affects the amplitude of responses only, while have little effect on the location of peaks (or resonance periods). The m and K_m have influence on both amplitudes and locations of peaks. With m increasing, the location of peak moves to a larger T (line 1 vs. 2), while to a smaller T as K_m increasing (line 1 vs. 3). This validates that the resonance period of the DR-WEC is controllable by manipulating the sliding-mass and spring. Therefore, the DR-WEC is able to tune itself to match the wave encounter frequency to enhance the power absorption ability.

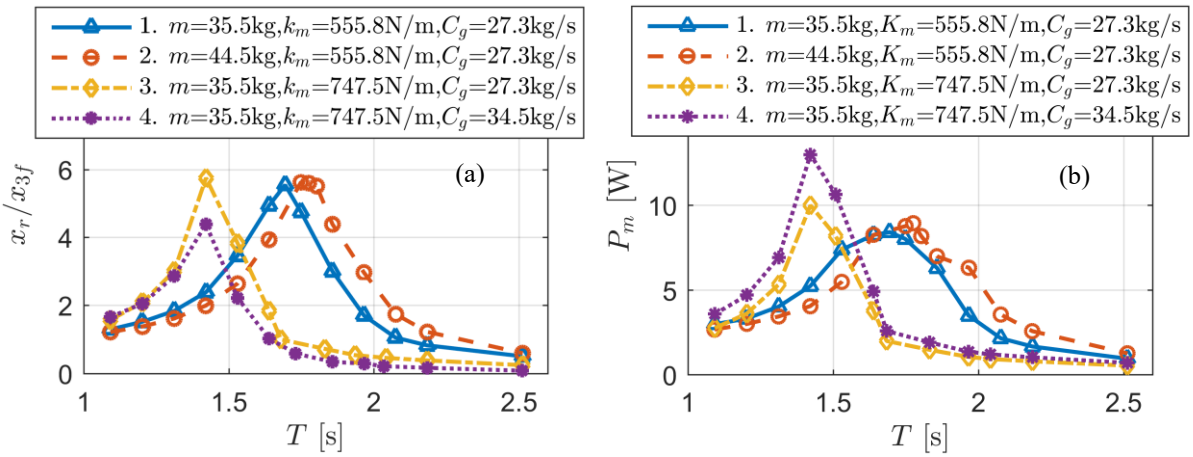

Fig.14. Motion (a) and power (b) responses for different PTO parameters.

5.2.2. Mechanical efficiency

The mechanical efficiency η of the BI-PTO with different parameters is shown in Fig.15. Generally, the variation of η for different PTO parameters is small. The average η of all cases is 65.8% with maximum

up to 80.0%. For different cases that from 1 to 4 in Fig.15, the mean η is 70.4%, 64.1%, 62.6%, and 66.0%, respectively. From the comparisons of "line 1 vs. 2" and "line 1 vs. 3", it reveals that a larger sliding-mass or spring constant leads to a lower efficiency. This is because the mechanical friction is larger when the gravity force of the sliding-mass or the spring force is larger. For a larger C_g, the mechanical efficiency is larger. The reason is that the varying of the damping system has little effect on the value of the mechanical friction, so that η increases as C_g increases from Eq.(11). The energy loss comes from the mechanical friction. With a better processing technology and bearings with smaller friction coefficients, the mechanical efficiency η could have a further increase.

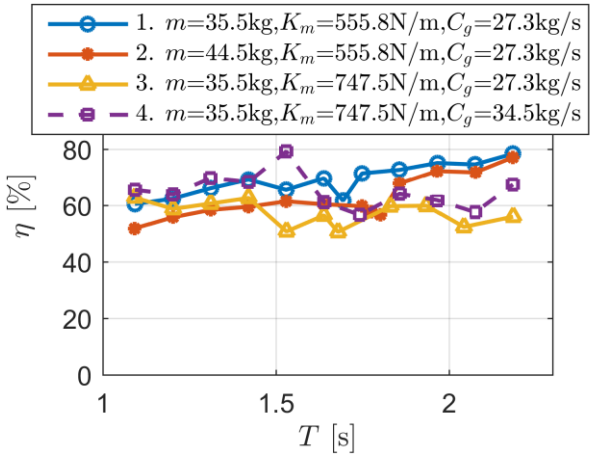

Fig.15. The test results of the mechanical efficiency for different PTO parameters.

5.3. Wave tank experiment for the DR-WEC

5.3.1. Viscous added mass and damping

The numerical and experimental studies conducted by Tom [24] and Son et al. [25] demonstrated that the excitation forces could be well predicted by the linear potential flow theory, while the radiation forces (especially the damping term) are significantly affected by the viscous effect. Therefore, the viscous effect should be studied mainly on the radiation force. The detailed derivation of the linearized viscous corrections from the free decay curves can be found in [26]. Here we only introduce in the expression of the non-dimensional linearized viscous corrections

$$\begin{cases} \overline{f}_{\mu,vis} = \mu_{vis} / \mu_{33} \\ \overline{f}_{\lambda,vis} = \lambda_{vis} / \lambda_{33} \end{cases} \tag{19}$$

where μ_{33}, λ_{33} are the potential added mass and radiation damping which are calculated by AQWA in frequency domain based on the Boundary Element Method (BEM). μ_{vis} and λ_{vis} denote the linearized added

mass and damping in the viscous fluid, respectively. The physical meaning of $\bar{f}_{\mu,vis}$ and $\bar{f}_{\lambda,vis}$ shows the ratio of the linearized viscous added mass or damping and the potential added mass or damping.

To achieve the free decay curve of the outer-floater in heave, the experiment was set up as shown in Fig.16. In the free decay test, the internal mass, which was fixed at the lowest point of its stroke, acted like a ballast. Therefore, all parts of the BI-PTO could not move during the free decay test. Firstly, we made the outer-floater float on the designed water line. Then, the suspension bridge was lifted with a distance x_{30}, and the position was kept to make sure the initial velocity to be zero. Next, the lifting rope was quickly cut down to let the outer-floater free decay in heave. In this experiment, the initial excursion x_{30} was set as 0.25m. The free decay curve is shown in Fig.17, the resonance frequency is 1.8s. The viscous added mass and damping correction coefficients are $\bar{f}_{\mu,vis}$=1.21 and $\bar{f}_{\lambda,vis}$=1.93, respectively.

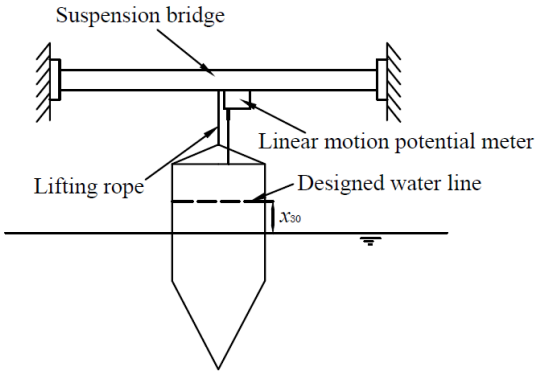

Fig.16. Schematic of the free decay test.

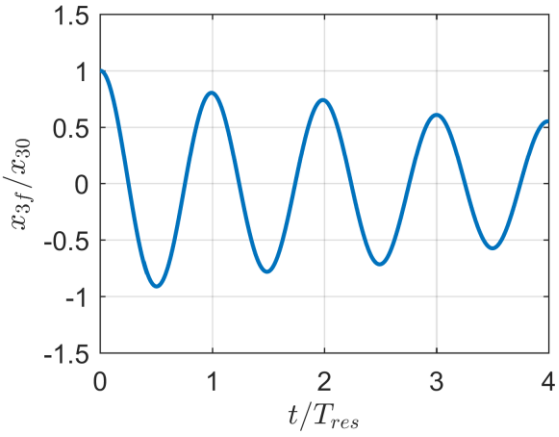

Fig.17. Free decay curve of the outer-floater.

5.3.2. Motion and power response

As shown in Fig.18, the test model of the DR-WEC was set in the middle of the wave tank and a single point mooring system was attached to the tip of the conical bottom. The motions of the outer-floater and the internal mass were captured by a visual motion measurement system, QUALISYS [27].

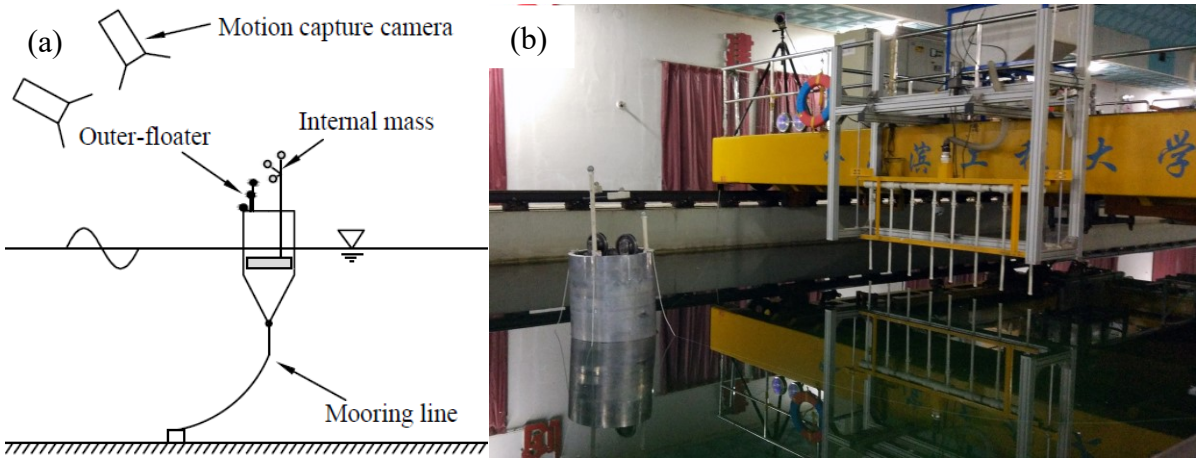

Fig.18. Schematic (a) and photograph (b) of the arrangement of the wave excitation experiment.

Firstly, we fixed the internal mass with the outer-floater, so that the whole system became one rigid floating body. The Response Amplitude Operator (RAO) of the outer-floater is shown in **Error! Reference source not found.**. With viscous effect correction achieved by the free decay test (Section 5.3.1), the numerical results match very well with the experimental measurements. This reveals that the viscous correction derived from the free decay test can be used in the prediction of the floater motion under linear wave condition with acceptable accuracy.

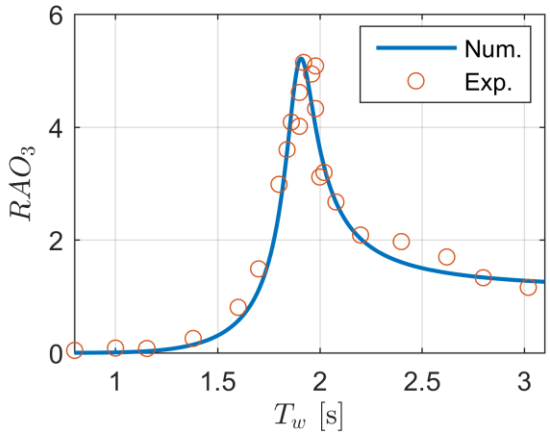

Fig.19. Comparison of the outer-floater RAO between numerical and experimental results

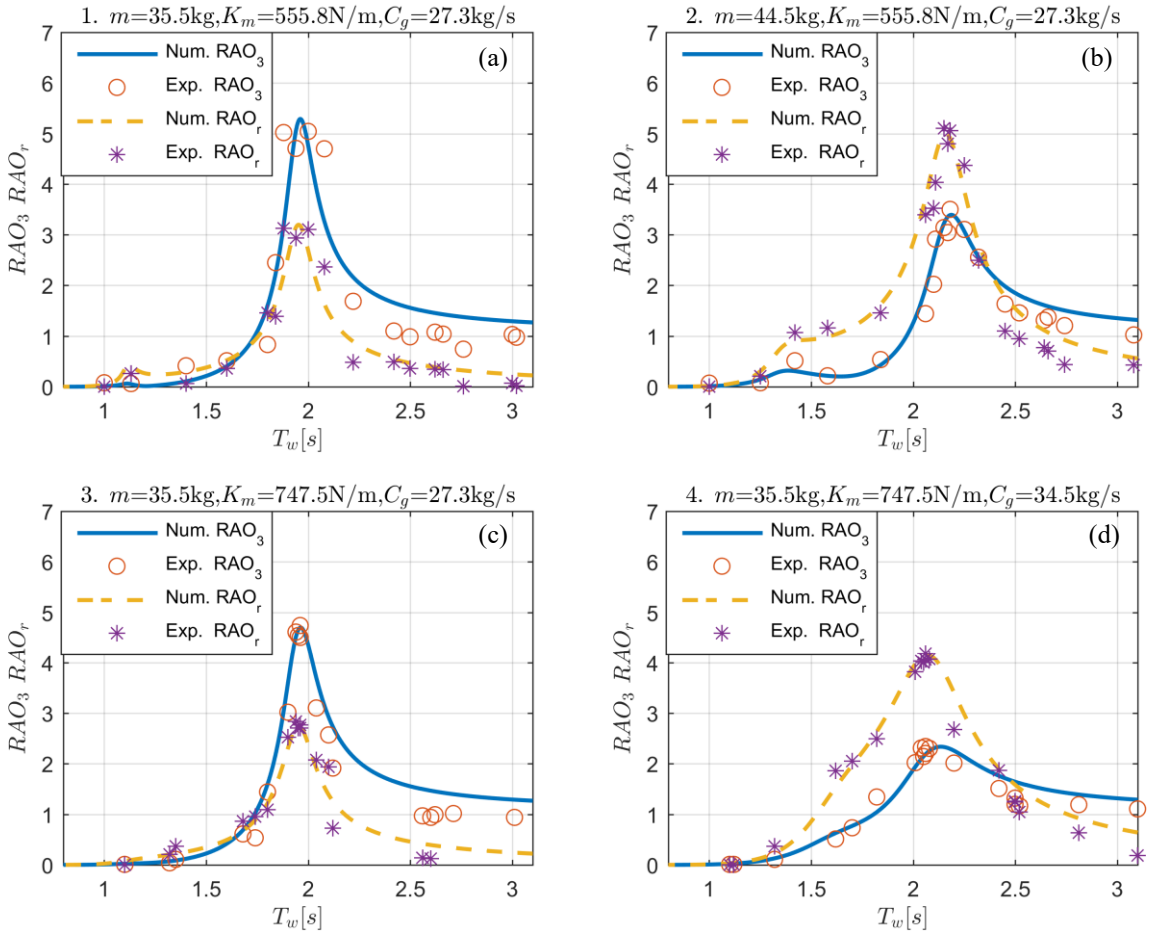

Fig.20. Comparison of the motion responses (outer-floater motion and internal-mass relative motion RAOs) between numerical and experimental results for different cases 1 to 4 (a ~ d) which have same PTO parameter as in bench test (Fig.14).

Next, we set the internal mass, spring, and damping to different values (same as in the bench test, i.e. Fig.14) to test the motion and power response. As shown in Figs. 20 and 21, the numerical results match well with the experimental results. It has demonstrated that to simulate the motion and power response of the DR-WEC with reasonable accuracy, the mechanical added mass and viscous corrections are essential for the numerical simulation (Eq.(14)), while the effect of mooring system or other degree of freedom (surge, pitch, etc.) can be ignored.

In this experiment, the outer-floater is connected with a slack single point mooring system (as shown in Fig.18). The mooring line is a 3.0mm Dyneema polyester rope. The purpose is to keep the model in position. We have tested that if we remove the mooring system, whether the changes on the motion and power response in heave is trivial. We have found out that the only difference is that the model is floating

away due to the drift force. As the model is axisymmetric and excited by regular waves, the motions in yaw, sway, and roll are very small. The major degree of freedoms (DOFs) are heave, surge, and pitch. The heave is the working DOF, while the surge and pitch are nauseous. Fortunately, the pitch and surge motions are small during the test. Example of the surge x_{1f} and pitch x_{5f} response can be found in Fig.22 (m=35.5kg, K_m=555.8N/m, C_g=27.3kg/m).

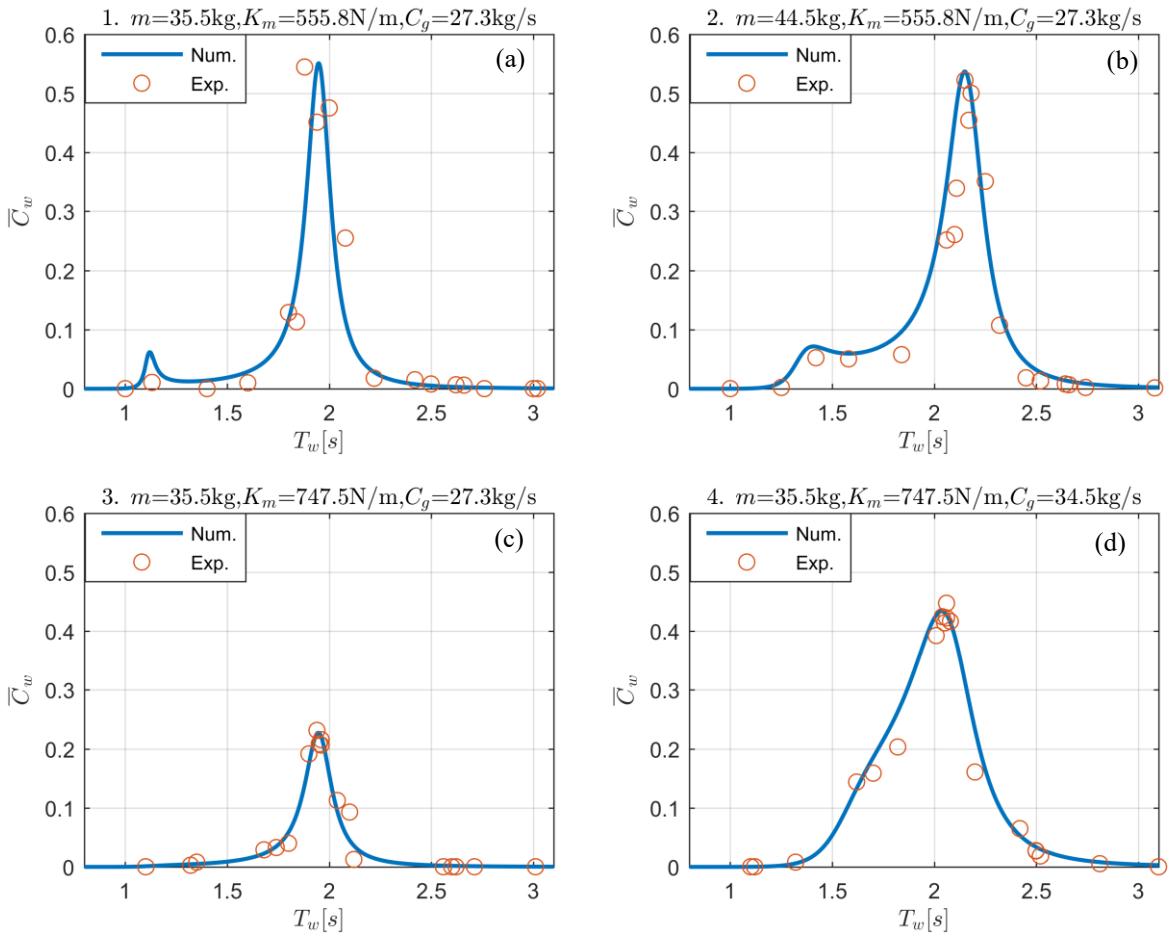

Fig.21. Comparison of the motion responses (outer-floater motion and internal-mass relative motion RAOs) between numerical and experimental results for different cases 1 to 4 (a ~ d) which have same PTO parameter as in bench test (Fig.14).

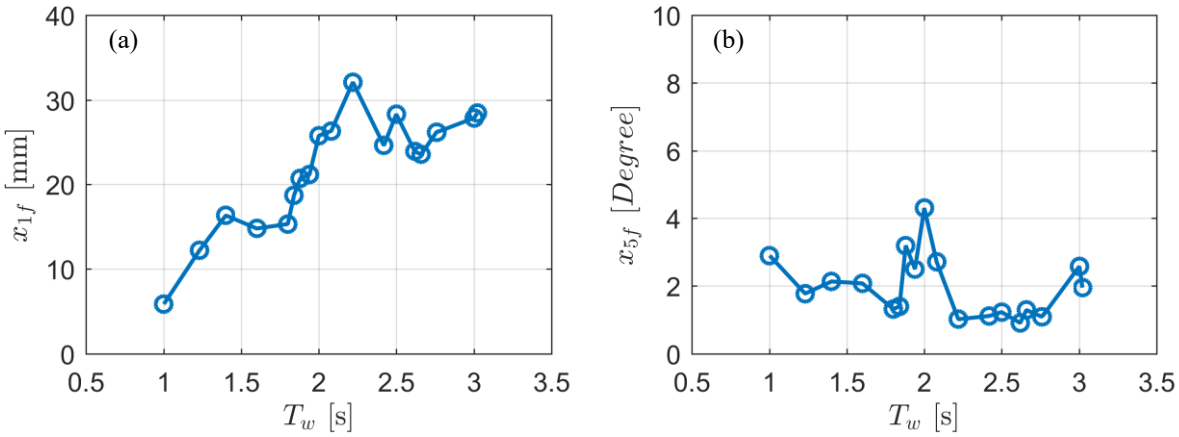

Fig.22. The surge (a) and pitch (b) response of the outer-floater under regular waves, when m=35.5kg, K_m=555.8N/m, C_g=27.3kg/m.

6. Conclusion

A point-absorber wave energy converter with a PTO system built inside a water-proof outer-floater, named DR-WEC, is presented in this paper. Through all the above numerical and experimental studies, the conclusions can be drawn as follows.

(1) The built-in PTO (BI-PTO) mechanism including sliding-mass, damping and spring systems specially for the DR-WEC is designed, where the spring system consisted of a fixed tension spring, wire ropes, and a stepped pulley is the most complicated because of the following three limitations practically. First of all, the fixed spring should be in tensile state all the time. Moreover, the allowable elongation of the fixed spring should be large enough. Finally, the original length of the fixed spring should be small enough due to the limited vertical space.

(2) The mechanical performance of the BI-PTO is tested and validated on a special designed test-bench. The parameters of the BI-PTO are controllable during the test. The damping can only affect the amplitudes of motion and power response, while the sliding-mass and spring have influences on not only the amplitudes of the motion and power response but also the resonance frequencies. The extra inertia effect, which comes from the moving parts (except the sliding-mass) of the BI-PTO, is represented as the mechanical added mass. This inertia effect couples the inertia forces (the outer-floater and the sliding-mass) in the motion equation, increases the resonance period, and reduces the maximum amplitudes of motion and power response. The

mechanical added mass has a negative influence on the power response so that it should be made as small as possible.

(3) The viscous effect for the DR-WEC during the motion in waves is mainly associated with the radiation force. The linearized viscous correction can be derived by free decay test. For the outer-floater used in this study, the corrections are $\bar{f}_{\mu,vis}$=1.21 and $\bar{f}_{\lambda,vis}$=1.93 respectively.

(4) The linear numerical model is put forward, the predicted heave motion and power response of the DR-WEC are found to be in good agreement with the experimental measurements in the wave tank tests. This has shown that the mechanical added mass and viscous corrections are essential for the numerical simulation with reasonable accuracy, while the effect of mooring system and other degree of freedoms (surge, pitch, etc.) can be ignored.

7. Acknowledgement

The authors gratefully acknowledge the financial support from the National Natural Science Foundation of China (51761135013), the High Technology Ship Scientific Research Project from Ministry of Industry and Information Technology of the People's Republic of China–Floating Security Platform Project (the second stage, 201622), the Fundamental Research Fund for the Central University (HEUCF180104, HEUCFP201809), the Open Fund of Key Laboratory of Renewable Energy, Guangzhou Institute of Energy Conversion, Chinese Academy of Sciences (Y707k51001), and the China Scholarship Council (the International Clean Energy Talent Programme, 2017).

References

[1] Falcão AFO, Henriques JCC. Oscillating-water-column wave energy converters and air turbines: a review. Renew Energy, 2016;85:1391-1424.

[2] Drew B, Plummer AR, Sahinkaya MN. A review of wave energy converter technology. Proc Inst Mech Eng Part A-J Power Energy 2009;223:887-902.

[3] Penalba M, Ringwood JV. A review of wave-to-wire models for wave energy converters. Energies, 2016;9:506.

[4] Mustapa MA, Yaakob OB, Ahmed YM, Rheem CK, Koh KK, Adnan FA. Wave energy device and breakwater integration: a review. Renew Sus. Energ Rev 2017;77:43-58.

[5] Uihlein A, Magagna D. Wave and tidal current energy – a review of the current state of research

beyond technology. Renew Sus. Energ Rev 2016;58:1070-1081.

[6] Mccabe AP, Aggidis GA. Optimum mean power output of a point-absorber wave energy converter in irregular waves. Proc Inst Mech Eng Part A-J Power Energy 2009;223:773-781.

[7] Wu S, Liu C, Chen X. Offshore wave energy resource assessment in the East China Sea. Renew Energy 2015;76:628-636.

[8] Babarit A, Ahmed HB, Clément AH, Debusschere V, Duclos G, Multon B. Simulation of electricity supply of an atlantic island by offshore wind turbines and wave energy converters associated with a medium scale local energy storage. Renew Energy 2006;31:153-160.

[9] Cordonnier J, Gorintin F, Cagny AD, Clément AH, Babarit A. Searev: case study of the development of a wave energy converter. Renew Energy 2015;80:40-52.

[10] Boren BC, Vertical axis pendulum wave energy converters: investigating control strategies and the deployment of a scaled generic prototype. Oregon State College of Engineering, Dissertations & Theses 2015.

[11] Kramer MM, Pecher AFS, Guaraldi I, Andersen MT, Kofoed JP. Hydraulic evaluation of Joltech's GyroPTO for wave energy applications. Dce Technical Reports, Aalborg University, 2015.

[12] Mccabe AP, Bradshaw A, Meadowcroft JAC, Aggidis G. Developments in the design of the PS Frog Mk 5 wave energy converter. Renew Energy 2014;31:141-151.

[13] Manninen J, Design of a testing system for a power take-off unit of a wave energy converter converter. Aalto University, Dissertations & Theses 2016.

[14] Ning DZ, Zhao X, Göteman M, Kang HG. Hydrodynamic performance of a pile-restrained WEC-type floating breakwater: an experimental study. Renew Energy 2016;95:531-541.

[15] Son D, Belissen V, Yeung RW. Performance validation and optimization of a dual coaxial-cylinder ocean-wave energy extractor. Renew Energy 2016;92:192-201.

[16] Liu Z, Shi H, Cui Y, Kim K. Experimental study on overtopping performance of a circular ramp wave energy converter. Renew Energy, 2017;104:163-176.

[17] Allen J, Sampanis K, Wan J, Greaves D, Miles J, Iglesias G. Laboratory tests in the development of wavecat. Sustainability 2016;8:1339.

[18] Dellicolli V, Cancelliere P, Marignetti F, Distefano R, Scarano M. A tubular-generator drive for wave energy conversion. IEEE Trans Ind Electron 2006;53:1152-1159.

[19] Lasa J, Antolin JC, Angulo C, Estensoro P, Santos M, Ricci P. Design, construction and testing of a hydraulic power take-off for wave energy converters, Energies 2012;5:2030-2052.

[20] Antolín-Urbaneja JC, Cortés A, Cabanes I, Estensoro P, Lasa J, Marcos M. Modeling innovative power take-off based on double-acting hydraulic cylinders array for wave energy conversion. Energies 2015;8:2230-2267.

[21] Jin S, Patton R. Geometry influence on hydrodynamic response of a heaving point absorber wave energy converter. European Wave and Tidal Energy Conference 2017.

[22] Li JF, Song G, Wang K, Yin S, Fang Z. Damping features analysis of stroke-related variable damping hydraulic shock absorber. Mach Tool Hydraul 2016;44:38-41

[23] Bachynski EE, Young YL, Yeung RW. Analysis and optimization of a tethered wave energy converter in irregular waves. Renew Energy 2012;48:133-145.

[24] Tom NM, Design and control of a floating wave energy converter utilizing a permanent magnet linear generator. PhD Thesis, University of California, Berkeley 2013.

[25] Son D, Belissen V, Yeung RW, Performance validation and optimization of a dual coaxial-cylinder ocean-wave energy extractor. Renew Energy 2016;92:192-201.

[26] Chen ZF, Zhou BZ, Zhang L, Zhang WC, Wang SQ, Geometrical Evaluation on the Viscous Effect of Point-Absorber Wave-Energy Converters, China Ocean Eng 2018;32:443-452.

[27] Zhuang K, Ping LI, Model test investigation on vortex-induced motions of a buoyancy can. Marine Structures, 2017;53:86-104.

Appendix A

Starting from the equation of motion on the bench Eq.(5), and assuming all motions are harmonic.

$$\begin{cases} x_{3f} = \hat{x}_{3f} e^{i\omega t} = \left|\hat{x}_{3f}\right| e^{i\left(\omega t + \varphi_{3f}\right)} \\ x_r = \hat{x}_r e^{i\omega t} = \left|\hat{x}_r\right| e^{i\left(\omega t + \varphi_r\right)} \end{cases} \tag{A.1}$$

Put Eq.(A.1) into Eq.(5)

$$-\omega^2\left(m+\mu_{mech}\right)\hat{x}_r e^{i\omega t} - \omega^2 m \hat{x}_{3f} e^{i\omega t} = -C_{total} i\omega \hat{x}_r e^{i\omega t} - k_m \hat{x}_r e^{i\omega t} \tag{A.2}$$

Then,

$$\frac{\hat{x}_{3f}}{\hat{x}_r} = \frac{-\omega^2\left(m+\mu_{mech}\right) + i\omega C_{total} + k_m}{\omega^2 m} \tag{A.3}$$

The upper equation can also be expressed in the form of

$$\frac{\left|\hat{x}_{3f}\right|}{\left|\hat{x}_r\right|} e^{i\left(\varphi_{x3} - \varphi_{xr}\right)} = \frac{-\omega^2 \mu_{mech} + k_m}{\omega^2 m} - 1 + i\frac{C_{total}}{\omega m} \tag{A.4}$$

For Eq.(A.4), the real part and the imaginary pare of the left- and right-hand-side should be equal correspondingly

$$\begin{cases} \dfrac{-\omega^2 \mu_{mech} + k_m}{\omega} - \omega m = \omega m \dfrac{\left|\hat{x}_{3f}\right|}{\left|\hat{x}_r\right|} \cos\left(\varphi_{3f} - \varphi_r\right) \\ C_{total} = \omega m \dfrac{\left|\hat{x}_{3f}\right|}{\left|\hat{x}_r\right|} \sin\left(\varphi_{3f} - \varphi_r\right) \end{cases} \tag{A.5}$$

Finally, we can derive the expression of the total damping from Eq.(A.5).

$$C_{total} = \omega m \frac{\left|\hat{x}_{3f}\right|}{\left|\hat{x}_r\right|} \sqrt{1 - \left[\left(\frac{-\omega^2 \mu_{mech} + k_m}{\omega^2 m} - 1\right) \frac{\left|\hat{x}_r\right|}{\left|\hat{x}_{3f}\right|}\right]^2} \tag{A.6}$$

In Eq.(A.6), m and K_m are given by the measurement. μ_{mech} can be calculated by Eq.(8). Consequently, the total damping can be calculated as long as we know the frequency and amplitudes of the motions ($\left|\hat{x}_{3f}\right|$ and $\left|\hat{x}_r\right|$) which can be measured by the bench test.